

Published in final edited form as:

Int J Imaging Syst Technol. 2012 March 1; 22(1): 44–52. doi:10.1002/ima.22001.

Background and Mathematical Analysis of Diffusion MRI

Methods

Alpay Özcan^{a,1}, Kenneth H. Wong^a, Linda Larson-Prior^b, Zang-Hee Cho^c, and Seong K. Mun^a

^aHealth Research, Arlington Innovation Center, Virginia Polytechnic Institute and State University, 900 N. Glebe Road, Arlington VA, 22203, USA

^bWashington University School of Medicine, Department of Radiology, Campus Box 8225, 4525 Scott Ave., St. Louis, MO 63110 USA

^cNeuroscience Research Institute, Gachon University of Medicine and Science, 1198 Guwol-dong, Namdong-gu, Incheon, Republic of Korea 405-760

Abstract

The addition of a pair of magnetic field gradient pulses had initially provided the measurement of spin motion with nuclear magnetic resonance (NMR) techniques. In the adaptation of DW-NMR techniques to magnetic resonance imaging (MRI), the taxonomy of mathematical models is divided in two categories: model matching and spectral methods. In this review, the methods are summarized starting from early diffusion weighted (DW) NMR models followed up with their adaptation to DW MRI. Finally, a newly introduced Fourier analysis based unifying theory, so-called Complete Fourier Direct MRI, is included to explain the mechanisms of existing methods.

Keywords

Nuclear Magnetic Resonance; Magnetic Resonance Imaging; Diffusion; Diffusion Weighted Imaging; Fourier Transform

1. Introduction

Nuclear magnetic resonance (NMR) and investigation of diffusion phenomenon have led to important physical and mathematical discoveries [1] in the twentieth century; the discovery of material properties via NMR spectroscopy and advances in the theory of stochastic processes respectively to name two. These research areas come together in the analysis of the effect of spin diffusion on NMR signal. As the spins move in a magnetic field gradient (i.e. a changing magnetic field strength dependent on position) their magnetization vector changes individually according to their paths. This was accounted for in different manners by the pioneers of NMR: Hahn's [2] description of diffusing spins' effects in spin echo experiment followed by Carr and Purcell's [3] random walk approach and Torrey's incorporation of magnetization diffusion [4] to Bloch equations. Torrey utilized a partial differential equation (PDE) framework instead of particle methods used by Hahn and, Carr and Purcell.

In Torrey's work [4], the effects of diffusion on NMR signal "under conditions of inhomogeneity in magnetic field" [4] were mathematically formulated. Shortly thereafter,

¹Correspondence to: Alpay Özcan, alpay@vt.edu.

moving one step further Stejskal and Tanner *intentionally* introduced a pair of (homogenous) magnetic field gradients into the spin echo experiment with the purpose of accurately measuring the scalar diffusion coefficient of the sample under investigation [5]. When spins diffuse in a magnetic field gradient their transverse magnetizations disperse because the gradients or inhomogeneity creates a different magnetic field strength at each location. This changes the rotational speed of each magnetization vector according to its spin's diffusion path. Each spin possess a different path thereby creating the dispersion of the magnetization. In the particle method framework, this principle was also analyzed by McCall et al. [6] with a statistical approach that refined Hahn's [2] magnetization's phase distribution formulation but departing from the random walk model of Carr and Purcell [3].

Although the pair of magnetic field gradient pulses are conventionally named as diffusion sensitizing gradients in the pulsed gradient spin echo experiment (PGSE) of Stejskal and Tanner, they do in fact encode spin motion regardless of its coherence or lack thereof [7]. In a sense, diffusion NMR has introduced the motion information as an additional dimension before magnetic resonance imaging (MRI) increased dimensionality with addition of position of spins as an independent variable. Nevertheless, the techniques involving diffusion sensitizing gradients whether for NMR spectroscopy or MRI are called diffusion weighted (DW) methods.

Decades later, the DW technique has been adapted to MRI with great success, with early detection of ischemia [8] being a very important example. Investigations were based on the estimation of a scalar descriptor, the so-called apparent diffusion coefficient (ADC) which represents the equivalent of isotropic diffusivity in an anisotropic environment. In other words, environments allowing unrestricted and restricted motion of molecules are compared with ADC. DW magnetic resonance (MR) measurement of anisotropy caused by three dimensional microstructure's alteration of spin motion raised an opportunity to infer more detailed information, specifically about biological tissue. Furthermore, researchers took advantage of MRI hardware's capability of producing vectorial magnetic field gradients. They developed models to express characteristics of spin motion as three dimensional constructs which traversed beyond the scalar (apparent) diffusion coefficient's potential. The most widely known of these models are perhaps the q-space formalism [9] and diffusion tensor imaging (DTI) [10, 11]. Whereas the former builds a Fourier framework between DW-MR signal and spin displacement properties, the latter projects the signal onto an ellipsoid, mathematically described by a symmetric tensor of rank two (which is a quadratic form).

These developments have pushed the initial utilization of ADC to different crucial areas in research and clinical imaging: early clinical diagnosis of ischemia [12], cancer diagnosis [13, 14] follow-up on treatment, pre- and post-operative assessment for different organs (e.g., fiber tracking [15, 16] before brain surgery [17]), monitoring of neurological diseases and disorders [18, 19], neonatal development [20] and traumatic brain injury [21]. In consequence, DW-MRI is now an indispensable and versatile tool, widely used in research with an increasing number of accepted clinical applications.

2. Diffusion Weighted Models for NMR Spectroscopy

2.1 Partial Differential Equations

The mathematical treatment of the diffusion MR signal is confined traditionally to a partial differential equation (PDE) framework which is used for both diffusion [22] and Bloch equations. The starting point is Fick's first equation that describes the rate of transfer, J , of diffusing magnetization, M , through the unit area in each direction where D is the diffusion coefficient:

$$J = -D\nabla M \quad \text{Equation 1}$$

Whereas Torrey [4] leaves the scalar diffusion coefficient, D , as position dependent (thereby covering a more general case), Stejskal and Tanner [5] following Abragam's formulation [23] treat it as position independent in Fick's second equation [22] allowing the commutation of operators in the diffusion equation,

$$\frac{\partial M}{\partial t} = \nabla \cdot D\nabla M \rightarrow \frac{\partial M}{\partial t} = D\nabla^2 M \quad \text{Equation 2}$$

(t denotes time). This formulation, valid for unrestricted diffusion, as in a liquid sample, describes the Brownian motion. Accordingly, Brownian motion is mathematically modeled by Wiener process which is defined as the stochastic process with Gaussian distributed independent increments. By this property the Wiener process equivalently satisfies the Markovian property [24]. In other words, the spins in Brownian motion are memoryless, their future positions do not depend on their position history. On the other hand, the obstacles posed by microstructure determine the future of spin motion according to past spin interactions with microstructure. Therefore the inclusion of Markovian property is not necessarily adequate in describing molecular motion in a restricted environment where past positions shape the future motion².

Nevertheless, the Bloch-Torrey equation, which phenomenologically describes NMR, takes this form after neglecting relaxation effects:

$$\frac{\partial M}{\partial t} = \gamma M \times B + D\nabla^2 M, \quad \text{Equation 3}$$

with γ and B denoting the gyromagnetic ratio and the magnetic field respectively. Proceeding with the solution Bloch-Torrey equation for PGSE, Stejskal and Tanner rigorously obtained the characterization of the DW signal attenuation of the free induction decay's (FID) magnitude as:

$$S_i = S_0 \exp(-bD) \quad \text{Equation 4}$$

Here S_i denotes the magnitude of the FID corresponding to the acquisition using the i^{th} diffusion sensitizing gradient magnitude with $i=0$ indicating the absence of diffusion sensitizing gradients (see Figure 1) and b is derived using the duration, δ , the separation, Δ , times of the (rectangular) diffusion sensitizing gradients and the magnitude of the diffusion sensitizing gradient pulse g [5]:

$$b = \gamma^2 \delta^2 \left(\Delta - \frac{1}{3} \delta \right) g^2. \quad \text{Equation 5}$$

Basically, the attenuation is characterized as a Gaussian function of diffusion gradient strength g . The diffusion coefficient and the diffusion gradient times define the shape of the Gaussian.

²In the investigations of microstructured environments, this is the reason the term 'apparent' appears in front of diffusion coefficient, which is defined for environments that allow unrestricted or isotropic motion.

2.2 Displacement Probabilities

Before the appearance of Torrey's PDE approach [4], initial modeling of diffusion NMR in spin echo experiments by Hahn [2] was based on the expression of the distribution of individual spins' transverse magnetization phase. Carr and Purcell [3] interpreted diffusion using a random walk model to arrive at Hahn's result for signal attenuation:

$$S_i = S_0 \exp\left(-\frac{2}{3} \gamma^2 g^2 T_e^3 D\right). \quad \text{Equation 6}$$

Unlike in the case of PGSE experiment, g represents here a constant magnetic field gradient rather than the strength of pulsed gradients of Figure 1.

Around the publication time of Stejskal and Tanner's seminal work [5], another less noticed work treating diffusion NMR signal via particle methods was published by McCall et al. [6]. The work departed from the random walk formulation of Carr and Purcell [3] which records the phase of the transverse magnetization during each random walk step in a magnetic field gradient. The analysis of McCall et al. [6] returned to the initial statistical treatment of Hahn [2] describing the magnetization phase distribution caused by spin motion. Despite minor mathematical discrepancies³, the fruitful idea refines Hahn's [2] analysis by expressing the individual phase directly as a function of spin displacements and obtains exactly Equation 6.

More than two decades after the publication of McCall et al. [6], Callaghan modeled the PGSE signal using techniques of scattering theory in the spirit of particle methods. In the model, an analogy between the probability of "finding any scattering center" [9] and the probability of spin displacements creates the so-called q-space model. With the narrow pulse assumption, i.e. negligible diffusion gradient pulse duration in comparison to the separation time, $\delta \ll \Delta$, Callaghan computes the amplitude of the echo at T_e as

$$E(G_D) = \int \rho(x) \int P_s(x', \Delta | x) \exp(i\gamma \delta G_D \cdot (x' - x)) dx' dx \quad \text{Equation 7}$$

with ρ and G_D denoting the spin density and the three dimensional diffusion sensitizing magnetic field gradient vector respectively. P_s is the probability of a particle initially at x to be found at x' after the pulse separation time, Δ . Relying on Markovian property, Callaghan rewrites Equation 7 using the "dynamic displacement": $R = x' - x$, and the average propagator [9], $\bar{P}(R, \Delta)$, which "gives the average probability for any particle to have a dynamic displacement R over a time Δ " [9]. Accordingly the signal at echo time is calculated as:

$$E(q) = \int \bar{P}(R, \Delta) \exp(i2\pi q \cdot R) dR, \quad \text{Equation 8}$$

where $q = (2\pi)^{-1} \gamma \delta G$, giving the name q-space.

The derivations of these results are strongly dependent on the single point measurements at echo time (see Figure 1). However, the same reasoning is not applicable to DW-MRI for the reasons that will be explained in Section 4.

³The assertion that the integrals of sample paths of a Gaussian distributed stochastic process are Gaussian does not exist in the reference provided in the manuscript [25. M. E. Munroe, *Theory of probability*, McGraw-Hill, New York, 1951.]. In fact its proof does not exist in the literature to the best of the authors' knowledge.

Finally, it is worth pointing out that particle methods and PDE's are equivalent mathematically [26]. Accordingly, both PDE and particle methods based derivations are valid for DW methods.

3. Diffusion Weighted Magnetic Resonance Imaging Models

In comparison to NMR spectroscopy, MRI scanner hardware creates three dimensional magnetic field gradients that allow the measurement of spin density as a function of position. The spin density, usually weighted by relaxation times (T_1 , T_2) is presented as an image. In other words, as an improvement to obtaining an average measurement from the whole sample of NMR spectroscopy, MRI augments the signal dimensionality by adding positional information. Beginning in the late 1980s, diffusion methods were adapted to MRI using the mathematical models of DW-NMR described in Sections 2.1 and 2.2. An important leap occurred when researchers moved from the investigations of the scalar quantity (ADC) to the estimation of more general three dimensional geometric constructs. For example, DTI estimates ellipsoids defined by a quadratic form (diffusion tensor), D , which is basically a symmetric 3×3 matrix. The scalar quantity ADC is equal to the mean of the eigenvalues of the matrix D .

DW-MRI methods can be grouped under two general categories:

1. **Model Matching Methods** initiated by diffusion tensor imaging (DTI) [10, 11] and refined with high angular resolution diffusion-weighted imaging (HARDI) [27], composite hindered and restricted model of diffusion (CHARMED) [28], spherical deconvolution [29], diffusion orientation transform (DOT) [30] two versions of the generalized DTI (GDTI) [31, 32] and diffusional kurtosis imaging (DKI) [33].
2. **Spectral methods** originating from Callaghan's q-space [9] followed by the diffusion spectrum imaging (DSI) [34], Q-ball imaging [35].

3.1 Model Matching Methods

DW-MRI model matching methods are direct adaptations of signal attenuation modeling in DW-NMR spectroscopy. The models assume that images obtained with diffusion sensitizing gradients demonstrate different attenuation levels at different pixels as a function of diffusion gradient vectors. This reflects characteristics of spin motion dictated by the microstructure. The model matching method is described by the following generic equation adopted from Equation 4:

$$I_i = I_0 \exp(-H(G_{D_i})). \quad \text{Equation 9}$$

Here, the model is no longer for the FID but its Fourier transform, which is in the image domain: I_i is the intensity (magnitude in most cases) of a given pixel from the image obtained with the i^{th} diffusion gradient vector G_{D_i} . The methods are defined by the functional presentation of the model, H . The data are projected onto H which also incorporates the unknown to be estimated, namely the spin motion descriptor.

3.1.1 Diffusion Tensor Imaging—In the original formulation of model matching pioneering work, DTI [10, 11], the function is

$$H = B(G_{D_i}, \delta, \Delta) : D. \quad \text{Equation 10}$$

The descriptor is the diffusion tensor D to be estimated from the (now 3 dimensional) Bloch-Torrey equation (Equation 3). B is a matrix valued function of G_{D_i}, δ, Δ [11] and it multiplies D element by element. This formulation is refined to a natural linear algebraic framework by Papadakis et al. [36] who noticed that in fact

$$B(G_{D_i}, \delta, \Delta): D = \gamma^2 b_t G_{D_i}^T D G_{D_i}. \quad \text{Equation 11}$$

The constant coefficient $b_t = \delta^2 (\Delta - \frac{1}{3} \delta)$, introduced later in [37] delineates the gradient duration and separation times (δ, Δ) from their vector part G_{D_i} in contrast to b of Equation 5. Conventional diffusion gradient schemes (DGS, the list of diffusion sensitizing gradient vectors used in a DW experiment) are specified using a single b -value for the entire diffusion gradient vectors G_{D_i} ; thereby confining all of them onto a sphere. The introduction of b_t made possible the design of new DGS via optimization methods. In [38], the effect of imaging gradients is minimized with DGSs containing vectors of different magnitudes optimally placed with respect to the imaging magnetic field gradients.

At a basic level, Equation 11 implies that D estimated from DTI experiments is forcefully a symmetric matrix because for any vector, $G, G^T D G = G D^T G$ and

$$2G^T D G = G^T (D + D^T) G + G^T (D - D^T) G = G^T (D + D^T) G. \quad \text{Equation 12}$$

In other words, DTI can only measure the symmetric part of the diffusion tensor: $\frac{1}{2}(D + D^T)$. Symmetric matrices form a subspace and 3×3 symmetric matrices are represented as six dimensional vectors, $d = [d_1, d_2, d_3, d_4, d_5, d_6]$:

$$D = \begin{bmatrix} d_1 & d_4 & d_6 \\ d_4 & d_2 & d_5 \\ d_6 & d_5 & d_3 \end{bmatrix}. \quad \text{Equation 13}$$

This allows rewriting Equation 11 in a linear form following the steps of Papadakis et al. [36] and the refinements in [37]:

$$\gamma^2 b_t G_{D_i}^T D G_{D_i} = \gamma^2 b_t v_i d \quad \text{Equation 14}$$

with

$$v_i = [g_{ix}^2, g_{iy}^2, g_{iz}^2, 2g_{ix}g_{iy}, 2g_{iy}g_{iz}, 2g_{ix}g_{iz}] \quad \text{Equation 15}$$

where $G_{D_i} = [g_{ix}, g_{iy}, g_{iz}]$.

To solve for six elements of d , a minimum of six DW images plus one unattenuated image, I_0 , are acquired, $m \geq 6$ (see Figure 2) and the logarithm of Equation 9 is taken to give a set of linear equations:

$$\gamma^2 b_t V_g d = \gamma^2 b_t \begin{bmatrix} v_1 \\ \vdots \\ v_m \end{bmatrix} d = \begin{bmatrix} \ln(I_0) - \ln(I_1) \\ \vdots \\ \ln(I_0) - \ln(I_m) \end{bmatrix}. \quad \text{Equation 16}$$

The list of the gradient vectors used for the acquisition of DW images is called the diffusion gradient scheme (DGS) [39, 38, 40]. An example of DGS with the corresponding images is shown in Figure 2. It follows from elementary linear algebra that for Equation 16 to have a

$$V_g = \begin{bmatrix} v_1 \\ \vdots \\ v_m \end{bmatrix}$$

unique solution, the coefficient matrix, V_g , must have full rank. V_g is a function of DGS vectors (see Equation 15) and therefore the vectors must be chosen appropriately to guarantee the uniqueness of the solution. A set of mathematical necessary conditions for the choice of diffusion gradients that would guarantee the full rank condition were given in [37] a decade after the introduction of DTI.

Once the solution for d is found, the symmetric matrix D is reconstructed as in Equation 13 at each pixel. A standard theorem in linear algebra proves that symmetric matrices, thus the diffusion tensor, have orthogonal eigenvectors and real eigenvalues ($\lambda_1 \lambda_2 \lambda_3$). The setup is general in the sense that ADC can be calculated as the mean of the eigenvalues.

In this three dimensional structure, whereas the eigenvectors indicate the principal directions of the motion, corresponding eigenvalues describe the tendency of the spins to move in each direction. If all the eigenvalues are equal, the medium is isotropic as in a liquid. However, if the microstructure favors motion in a given direction, causing anisotropy, the eigenvalues will reflect that by differing from each other. Functions of the three eigenvalues describing their dispersion are called anisotropy measures, fractional anisotropy (FA) being one of the most used ones [41]:

$$FA = \frac{\sqrt{(\lambda_1 - \lambda_2)^2 + (\lambda_2 - \lambda_3)^2 + (\lambda_3 - \lambda_1)^2}}{\sqrt{2(\lambda_1^2 + \lambda_2^2 + \lambda_3^2)}} \quad \text{Equation 17}$$

Usually, an anisotropy map describing the microstructure is shown as an image with the value of anisotropy index at each pixel. The directional information might be added by displaying the eigenvector corresponding to the largest eigenvalue at each pixel as a 'whisker' (thus the name whisker plot). The directionality is also shown with a color image. A different color channel is assigned to each direction to display three components of the eigenvector accordingly. There are different applicable schemes depending on the properties of the spin motion [42]. The combined directional and motion tendency can also be shown by overlaying ellipsoids defined by the diffusion tensor ($x^T D x = \text{constant}$) on each pixel of an anatomic image. The equation of an ellipse requires that the eigenvalues of are all greater than or equal to 0. Otherwise, the diffusion equation, Equation 2, contradicts the conservation of mass. This physical constraint is sometimes violated in the estimation obtained from experimental DTI data. The reasons for the occurrences of negative eigenvalues from experimental data constitute currently an open question.

3.2 High Order Model Matching Methods

DTI can be considered as a second order approximation to the attenuation function H of Equation 9. Different expansions of the attenuation function result in different model matching methods. In high angular resolution diffusion-weighted imaging (HARDI) [27] the attenuation is expanded using the spherical harmonics Y_l^m [27]

$$H(G_{D_i}(\theta, \phi)) = \sum_{l=0}^{\infty} \sum_{m=-l}^l a_{lm} Y_l^m(\theta, \phi) \quad \text{Equation 18}$$

where (θ, ϕ) are the azimuthal and polar angles in the spherical coordinates. The coefficients, a_{lm} , are computed from Equation 18 using the experimental data. The odd numbered harmonics $l = 1, 3, 5 \dots$ are discarded on the basis that they are asymmetric [27].

A generalization of HARDI is provided by Tournier et al. in spherical deconvolution [29], utilizing concepts from linear systems theory with the use of a response function (also known as point spread function or transfer function in control theory) in spherical coordinates. The response function, equivalent to impulse response of a linear time invariant dynamical system, describes the signal originating from a single nerve fiber. In order to assess the distribution of multiple fibers within a voxel, the full set of measurements is deconvolved with the response function. The result is the fiber orientation density function.

In diffusional kurtosis imaging (DKI) [33], a higher order expansion using the concept of excess kurtosis is implemented. H is expanded by adding the kurtosis tensor to the diffusion tensor D [33]:

$$H(G_{D_i}) = \gamma^2 b_t G_{D_i}^T D G_{D_i} - \frac{ADC}{6} \gamma^4 b_t^2 D^{(4)}(G_{D_i}, G_{D_i}, G_{D_i}, G_{D_i}). \quad \text{Equation 19}$$

The kurtosis tensor $D^{(4)}$ is a symmetric tensor of rank 4 and the method is a generalization of DTI⁴. The expansion strategy of Equation 19 appeared before the work of Jensen et al. [33]. Özarslan and Mareci [31] integrated higher rank tensors into the Bloch-Torrey equations. The odd ranked tensor elements result in negative diffusion coefficients [31]. Özarslan and Mareci [31] argue that “since negative diffusion coefficients are non-physical, the rank is forced to be an even number” (see also the discussion about the negative eigenvalues in Section 3.1.1). Consequently the generalized diffusion tensor (GDT) approximation of H is given as:

$$H(G_{D_i}) = \gamma^2 b_t \sum_{n=1}^{\infty} D^{(2n)}, \quad \text{Equation 20}$$

The n arguments each of $D^{(n)}$ operates on is G_{D_i} , e.g. in the last term of Equation 19 where $n = 4$. About a year after the publication of [31], Liu et al. [32] published another GDT imaging model that incorporates higher order tensors of all ranks:

$$H(G_{D_i}) = \sum_{n=2}^{\infty} j^n \gamma^{2n} b_t^{(n)} D^{(n)}, \quad \text{Equation 21}$$

Where Equation $j = \sqrt{-1}$ and $b_t^{(n)}$'s are higher order integrals of the diffusion sensitizing gradient's time course. The inclusion of higher rank tensors is made possible by allowing the signal to be complex valued. In Equation 19, odd ranked tensors form the imaginary part of the signal. In addition, they are asymmetric terms and this covers physically a more general situation.

The general aim of these model matching methods is to estimate the descriptors of diffusion that would minimize the model matching error originating from the measurement values,

$$\widehat{I}_1, \dots, \widehat{I}_m;$$

⁴For example, D is a rank two tensor and both of its arguments are equal to G_{D_i} . Therefore, it is a quadratic form that can be represented as a matrix. Its value at G_{D_i} is found by left and right vector-matrix multiplication i.e. $D(G_{D_i}, G_{D_i}) = G_{D_i}^T D G_{D_i}$. Higher rank tensors have more complicated representations than vector-matrix multiplication.

$$\left\| \begin{bmatrix} \widehat{I}_1 \\ \vdots \\ \widehat{I}_m \end{bmatrix} - I_0 \begin{bmatrix} \exp(-H(G_{D1})) \\ \vdots \\ \exp(-H(G_{Dm})) \end{bmatrix} \right\|. \quad \text{Equation 22}$$

The solution of the minimization problem of Equation 22 for each model matching method results in the determination of a number of unknowns (e.g. 6 for DTI) specified by the model equations presented in this section. Naturally this number is also the minimum number of diffusion gradient vectors in DGS. Furthermore, in a parallel observation to the DTI estimation equations, the conditions on DGS guaranteeing the uniqueness of solution for different model matching methods have not been investigated and remain as an open and untouched subject of discussion.

In addition to the aforementioned methods that are using the attenuation model of Equation 9, there are two techniques that are compartmentalizing and approximating the q-space signal of Section 2.2. The first one, composite hindered and restricted model of diffusion (CHARMED) [28], divides the signal into two compartments as “hindered water diffusion in the extra-axonal space and restricted water diffusion in the intra-axonal space”. Accordingly the q-space signal originating from multiple compartments at the echo time is given as

$$E(q) = \sum_{i=1}^L f_h^i S_h^i + \sum_{j=1}^N f_r^j S_r^j \quad \text{Equation 23}$$

where “ L is the number of distinct hindered compartments and N is the number of distinct restricted components” [28], f_h^i and f_r^j are volume fractions of the compartments. Each of the compartments are further dissected to divide the signal into parallel and perpendicular (e.g. to axons) sections to obtain a final model. The second technique, diffusion orientation transform (DOT) of Özarlan et al. [30], takes the different path of expanding theoretically the Fourier Transform in Equation 9 using spherical harmonics. The propagator, \bar{P} of Equation 8, is expressed in the basis formed by the spherical harmonics. The expression, in essence, is the same as Equation 18 but it is the propagator, rather than the attenuation, that is approximated.

3.3 Spectral Methods

The basis of the spectral methods for DW-MRI is the adaptation of NMR q-space equation, Equation 8, to magnetic resonance imaging.[9]:

$$S(k, q) = \int \rho(x) E(q) \exp(i2\pi k \cdot x) dx, \quad \text{Equation 24}$$

where k is the usual MRI k-space variable and $E(q)$ is the adaptation of its NMR definition in Equation 7

$$E(q) = \int P_s(x', \Delta|x) \exp(i\gamma \delta G_D \cdot (x' - x)) dx'. \quad \text{Equation 25}$$

Clearly, in this equation $E(q)$ is a function of position x . Accordingly, it must be taken into account for the evaluation of the integral in Equation 24. To obtain Equation 24, on p.440 of [9] it is asserted that “despite the fact that both P_s and ρ may depend on x , the effect of the PGSE sequence is quite separable...”. It is also indicated that the signal comes from the finite volume element corresponding to the imaging voxel. In consequence, $E(q)$ should be

seen as “the Fourier transform of local dynamic profile” according to Equation 8.7, p.440, [9]:

$$E(q) = \int \bar{P}(R, \Delta) \exp(i2\pi q \cdot R) dR. \quad \text{Equation 26}$$

The goal of the method is the reconstruction of the average propagator using the Fourier transform from the measurements after their normalization. This is explicitly formulized in diffusion spectrum imaging (DSI) method of Wedeen (Equation 4, [34]):

$$\bar{P}(R, \Delta) = I_0^{-1} (2\pi)^{-3} \int I(q) |\exp(-i2\pi q \cdot R) dq. \quad \text{Equation 27}$$

Here, $I(q)$ is the (complex) pixel intensity corresponding to diffusion sensitizing gradient that produces q . In other words, $I(q) = I_i$ which is the image obtained with G_{D_i} such that $q = (2\pi)^{-1} \gamma \delta G_{D_i}$. The magnitude is taken “to exclude phase shifts arising from tissue motion” (paragraph preceding Equation 4, [34]). In DSI the main interest is the angular structure of the diffusion spectrum. The final product is the orientation distribution function defined as ‘a weighted radial summation of, $\bar{P}(R, \Delta)$ [34]:

$$ODF(u) = \int \bar{P}(ru, \Delta) r^2 dr \text{ with } \|u\| = 1 \text{ for } r > 0. \quad \text{Equation 28}$$

It is important to note the derivations in [34] rely on Markovian property and the narrow pulse approximation. Moreover, the magnitude of the signal is used on the basis that “the MRI signal is positive for any type of spin motion without net flux” [34]. Under these assumptions, the model is not completely unconstrained.

The Fourier reconstruction in general requires a large number of DW acquisitions compared to model matching methods. In DSI, the sampling of q-space is realized within a sphere. The issue of large number of acquisition is addressed by the use of the so-called Q-ball imaging (QBI) technique [35]. As in DSI, in QBI the quantity of interest is the orientation distribution function which is defined slightly different than DSI-ODF:

$$\psi(u) = \int \bar{P}(ru, \Delta) dr \text{ with } \|u\| = 1 \text{ for } r > 0. \quad \text{Equation 29}$$

By utilizing of the Funk-Radon transform (FRT), QBI estimates ψ with measurements obtained on a ball (hence the method’s name, QBI) in q-space, with significantly smaller number of acquisitions.

4. A Higher Dimensional Fourier Relationship

The methods described in previous sections are just representatives of many existing variations of DW-MR methods and techniques that were not listed here due to space restrictions. An exhaustive list can be found in the publication by Jian et al. [43] in 2007. The sheer number of methods could be considered as an indication of dissatisfaction with the performance of existing methods, especially originating from inadequacies that arise when identification of the microstructure of geometrically complex regions (e.g. fiber tract crossings) is attempted. One reason behind the inadequacy is the creation of DW-MRI models of Section 3 by direct adoption of DW-NMR models.

The following important considerations arise in the course of the adoption:

1. In contrast to DW-NMR, in MRI the signal does *not* originate from a single point at echo time (see Section 2). Even in MRI without diffusion weighting, all of the points in FID fill up the k-space and therefore all of them are necessary to construct the image or the volume.
2. Imaging gradients, which are naturally absent in NMR, are usually ignored in DW-MRI models. Attempts to integrate imaging gradient effects have unveiled significant problems in the derivation of DTI model [39]. Moreover, these problems cannot be remedied neither with optimization [38] nor with nonlinear estimation [40].
3. With the exception of Torrey's approach [4], D is treated as a position independent quantity within all of the models. For example, DTI relies on the assumption that "the diffusion coefficients are independent of space (position) within a voxel" (p. 253, [10]). Otherwise, DTI estimation equations cannot be derived. Position dependence complicates severely the solution of PDEs for DW imaging models.
4. The narrow pulse approximation is unrealistic. Considering that Wiener process has non-differentiable continuous sample paths, the irregularities of the spin motion are at a level of complexity which is unresolvable at any time scale regardless how short are the duration of the pulses.
5. With the exception of GDTI proposed by Liu et al. [32], the models obtain symmetric quantities either by projecting the data onto symmetric constructs (e.g. ellipsoids of DTI), pruning the asymmetric structures (see Section 3.2 with spherical harmonics of HARDI or odd ranked tensors of DOT) or by using the magnitude of the signal in spectral methods which forces the Fourier transform to result in (Hermitian) symmetric outcomes. An appropriate model must be unconstrained so that any property such as symmetry should be revealed by the data themselves establishing an evidence based methodology. Modeling presumptions constrain the outcome of the investigations.
6. Models rely on Markovian property which is not justifiable in restricted environments such as biological tissue (see Section 2.1).

Motivated by these concerns, a new accurate and unifying Fourier based theory of DW-MRI has been developed by returning to the first principles of DW-MR signal formation in [44, 45, 46]. The DW-MRI signal is modeled by expressing the evolution of the phase (Q_j) of the i^{th} spin's transverse magnetization,

$$m_i(t) = \exp(-j\gamma\Omega_i)t m_i(t_0) \quad \text{Equation 30}$$

(Equation 30 is the Bloch equation obtained when relaxations are neglected). The magnetization changes according to the displacement w_j from the initial position $x_i(t_0)$:

$$x_i(t) = x_i(t_0) + w_i(t), \quad \text{Equation 31}$$

because of the diffusion sensitizing magnetic field gradients (see Section 1). When the signal formation is derived for the PGSE experiment [44] using Equation 32 and Equation 33, the initial position $x_i(t_0)$ and the i^{th} spin's displacement integral, W_i^d ,

$$W_i^d = \int_{t_{d1}}^{t_{d2}} w_i(\tau) d\tau - \int_{t_{d3}}^{t_{d4}} w_i(\tau) d\tau, \quad \text{Equation 32}$$

(see Figure 1 for the definition of t_{di}) appear in the formulations. Furthermore, the derivations in [44] show that the complex valued DW-MRI signal that comes out of the MR scanner is the Fourier transform of the joint distribution of the number of spins starting from the initial position x and possessing W^d displacement integrals: $P_{\text{cfid}}(x, W^d)$

$$S_{\text{cfid}}(k_{\text{mr}}, k_{\text{D}}) = F[P_{\text{cfid}}(x, W^d)] \quad \text{Equation 33}$$

Accordingly, the method is named Complete Fourier Direct (CFD) MRI because the entire (complex valued) data constitute the Fourier transform of the distribution function $P_{\text{cfid}}(x, W^d)$. In Equation 33, the Fourier variables K_{mr} and K_{D} are the usual MR imaging k-space variable (read-out and slice select) and the diffusion sensitizing gradient vector $K_{\text{D}} = G_{\text{D}}$ respectively. Basically, CFD-MRI augments the dimension of MR imaging by adding, on top of position information of MRI (see also the discussion on paragraph 3 in Section 1), three more dimensions corresponding to displacement integrals. In contrast to the existing methods, the unifying CFD-MR framework does not separate position and displacement portions. In fact, in the derivations of CFD model, $P_{\text{cfid}}(x, W^d)$ comes up naturally as a joint distribution function.

It is very important to note that Equation 33 is the final product of intermediate steps that guarantee the preservation of S_{cfid} 's Hermitian symmetry [44]. This property is the only physical evidence at hand because the only known fact is that P_{cfid} is a real valued function being the count of (large but) finite number of spins. This implies that its Fourier transform in Equation 33 must be Hermitian,

$$S_{\text{cfid}}(k_{\text{mr}}, k_{\text{D}}) = S_{\text{cfid}}^*(-k_{\text{mr}}, -k_{\text{D}}) \quad \text{Equation 34}$$

(* denotes the complex conjugation).

P_{cfid} is reconstructed by taking the inverse Fourier transform of the entire data:

$$P_{\text{cfid}}(x, W^d) = F^{-1}[S_{\text{cfid}}(k_{\text{mr}}, k_{\text{D}})]. \quad \text{Equation 35}$$

CFD-MRI addresses the concerns raised in the beginning of this section as follows:

1. CFD-MRI calculations incorporate all of the data. The signal is not calculated from a single point but from all the points of augmented CFD k-space defined by $K_{\text{CFD}} = (K_{\text{mr}}, K_{\text{D}})$. K_{CFD} is either 5 or 6 dimensional depending on the slice or volume imaging is conducted. The last 3 dimensions come from 3 dimensional displacement integral vectors defined in Equation 32.
2. Imaging gradients are included by means of K_{mr} .
3. CFD-MRI expresses position dependence inherently in the first argument of joint distribution function $P_{\text{cfid}}(x, W^d)$ which is the initial position.
4. There is no need for the narrow pulse assumption. In Equation 32, the integrals are evaluated during the diffusion sensitizing gradient times.
5. The signal is treated as a complex valued quantity in contrast to using the magnitude. By preserving the Hermitian symmetry during the evaluation of Equation 35, asymmetry is allowed in $P_{\text{cfid}}(x, W^d)$. This guarantees an evidence based approach: if there is asymmetry or symmetry in the motion characteristics, data will show it.

6. The only assumption in Equation 31 is the continuity of the displacement w_i since a spin cannot disappear at one point and reappear at a different one. In addition, the displacement integral, W^d , is not a stochastic processes. Therefore any property thereof, such as being Markovian, is not needed to be in the model. Accordingly, CFD-MRI points out that the propagator is *not* the quantity that is being measured.

The simplicity of Equation 30 (Bloch equation) and Equation 31 (the most general equation of motion) make their combination tractable by use of particle methods. CFD-MRI model would be hard to derive using a PDE framework. However, theoretical equivalence of the two methods [26] indicates that particle method derivations are sufficient for modeling.

The Fourier relationship established with CFD-MRI clarifies the mechanisms of existing methods. For example, the Wiener process that describes self-diffusion in a liquid has displacements, W_i that are Gaussian distributed with 0 mean and covariance matrix equal to the diffusion tensor D . It can be derived after tedious but routine calculations that the displacement integrals, W_i^d , have mean equal to 0 and covariance equal to [45]

$$E \left[W_i^d (W_i^d)^T \right] = \delta^2 \left(\Delta - \frac{1}{3} \delta \right) D = b_t D. \quad \text{Equation 36}$$

This equation shows that the MR scanner acts as a filter on the diffusion process by scaling its covariance with b_t that only depends the duration and separation times of the diffusion sensitizing gradients. The DW signal that comes out of the scanner is the Fourier transform of the distribution.

Gaussians are eigenfunctions of the Fourier transform, i.e. the Fourier transform of a Gaussian is also a Gaussian [45]:

$$F \left[\exp \left((W_i^d)^T (b_t D)^{-1} W_i^d \right) \right] \cong \exp((k_D)^T (b_t D) k_D). \quad \text{Equation 37}$$

Equation 37 is key in understanding the model matching methods. Equation 9 is obtained by evaluating the Fourier transform in half of the variables, namely the imaging portion defined by K_{mr} and leaving the displacement integral portion K_D intact. In this mixed physical-frequency variable setup, the displacement portion remains on the Fourier domain. According to the right hand side of Equation 37, DTI estimates D in Fourier domain more easily than in the physical domain on the left side which involves of the inverse of D . In more complex microstructures, high order approximations follow the same strategy. They attempt to expand the mathematical Fourier transform by adding higher order terms described in Section 9 to the argument of the eigenfunction.

According to Equation 35, CFD-MRI reconstructs P_{cfid} using the inverse Fourier transform (discrete Fourier transform is used in practice). Spectral methods of Section 4 are based on the same principle but CFD evaluates the Fourier transform correctly (see Item 5 above), i.e. using complex valued signals. It obtains the correct distribution function (see item 6 above), in the sense that P_{cfid} being a joint distribution cannot necessarily be factored into a spin density and displacement descriptor. The mechanisms behind the methods are summarized in Figure 3.

5. Conclusion

All DW-MRI models process the data with the same goal in mind: non-invasive description of microstructural changes that will endow extraction of relevant information pertaining to diagnosis, prognosis and management of important health problems from different areas. The large number of models described herein is proof of continuing research effort in the quest of a more adequate model for DW-MRI. The unification of the plethora of approaches will improve the accuracy of the assessment provided by the modality. In this manuscript, the methods are summarized by describing their mathematical properties. In addition, they are interpreted using the Fourier based CFD-MRI method with the aim of reaching a consensus among the methods. An important future goal is the incorporation of these new findings into the tractography methods which is reserved for future studies.

Acknowledgments

Grant Sponsor: US Army grant, NeuroPerformance Imaging (W23RYX1089N603)

References

1. Mazo, RM. Brownian motion: Fluctuations, dynamics, and applications. Oxford University Press; 2002.
2. Hahn EL. Spin echoes. *Physical Review*. 1950; 80(4):580–594.
3. Carr HY, Purcell EM. Effects of diffusion on free precession in nuclear magnetic resonance experiments. *Physical Review*. 1954; 94(3):630–638.
4. Torrey HC. Bloch equations with diffusion terms. *Physical Review*. 1956; 104(3):563–565.
5. Stejskal EO, Tanner JE. Spin diffusion measurements: Spin echoes in the presence of a time-dependent field. *The Journal of Chemical Physics*. 1965; 42(1):288–292.
6. McCall DW, Douglass DC, Anderson EW. Self-diffusion studies by means of nuclear magnetic resonance spin-echo techniques. *Berichte der Bunsengesellschaft für Physikalische Chemie*. 1963; 67(3):336–340.
7. Nalcioglu O, Cho ZH. Measurement of bulk and random directional velocity fields by nmr imaging. *IEEE Trans Med Imaging*. 1987; 6(4):356–359. [PubMed: 18244045]
8. Moseley ME, Cohen Y, Mintorovitch J, Chileuitt L, Shimizu H, Kucharczyk J, Wendland MF, Weinstein PR. Early detection of regional cerebral ischemia in cats: Comparison of diffusion- and t2-weighted mri and spectroscopy. *Magn Reson Med*. 1990; 14(2):330–346. [PubMed: 2345513]
9. Callaghan, PT. Principles of nuclear magnetic resonance microscopy. Oxford University Press; Oxford [England] New York: 1991.
10. Basser PJ, Mattiello J, LeBihan D. Estimation of the effective self-diffusion tensor from the nmr spin echo. *J Magn Reson B*. 1994; 103(3):247–254. [PubMed: 8019776]
11. Mattiello J, Basser PJ, LeBihan D. Analytical expressions for the b matrix in nmr diffusion imaging and spectroscopy. *Journal of Magnetic Resonance Series A*. 1994; 108(2):131–141.
12. Baird AE, Warach S. Magnetic resonance imaging of acute stroke. *Journal of Cerebral Blood Flow and Metabolism*. 1998; 18(6):583–609. [PubMed: 9626183]
13. Xu J, Humphrey PA, Kibel AS, Snyder AZ, Narra VR, Ackerman JJ, Song SK. Magnetic resonance diffusion characteristics of histologically defined prostate cancer in humans. *Magn Reson Med*. 2009; 61(4):842–850. [PubMed: 19215051]
14. Song SK, Qu Z, Garabedian EM, Gordon JI, Milbrandt J, Ackerman JJ. Improved magnetic resonance imaging detection of prostate cancer in a transgenic mouse model. *Cancer research*. 2002; 62(5):1555–1558. [PubMed: 11888935]
15. Conturo TE, Lori NF, Cull TS, Akbudak E, Snyder AZ, Shimony JS, McKinstry RC, Burton H, Raichle ME. Tracking neuronal fiber pathways in the living human brain. *Proc Natl Acad Sci U S A*. 1999; 96(18):10422–10427. [PubMed: 10468624]

16. Mori S, van Zijl PC. Fiber tracking: Principles and strategies - a technical review. *NMR Biomed.* 2002; 15(7–8):468–480. [PubMed: 12489096]
17. Warfield SK, Talos F, Kemper C, Cosman E, Tei A, Ferrant M, Macq BMM, WMW, Black PM, Jolesz FA, Kikinis R. Augmenting intraoperative mri with preoperative fmri and dti by biomechanical simulation of brain deformation. *Proc SPIE.* 2003:77–86.
18. Budde MD, Kim JH, Liang HF, Russell JH, Cross AH, Song SK. Axonal injury detected by in vivo diffusion tensor imaging correlates with neurological disability in a mouse model of multiple sclerosis. *NMR Biomed.* 2008; 21(6):589–597. [PubMed: 18041806]
19. Ciccarelli O, Catani M, Johansen-Berg H, Clark C, Thompson A. Diffusion-based tractography in neurological disorders: Concepts, applications, and future developments. *The Lancet Neurology.* 2008; 7(8):715–727.
20. McKinstry RC, Mathur A, Miller JH, Ozcan A, Snyder AZ, Schefft GL, Almlı CR, Shiran SI, Conturo TE, Neil JJ. Radial organization of developing preterm human cerebral cortex revealed by non-invasive water diffusion anisotropy mri. *Cereb Cortex.* 2002; 12(12):1237–1243. [PubMed: 12427675]
21. Mac Donald CL, Johnson AM, Cooper D, Nelson EC, Werner NJ, Shimony JS, Snyder AZ, Raichle ME, Witherow JR, Fang R, Flaherty SF, Brody DL. Detection of blast-related traumatic brain injury in u.S. Military personnel. *The New England journal of medicine.* 2011; 364(22): 2091–2100. [PubMed: 21631321]
22. Crank, J. *The mathematics of diffusion.* Oxford University Press; 1975.
23. Abragam, A. *The principles of nuclear magnetism.* Clarendon Press; Oxford: 1961.
24. Shiriaev, AbN. *Probability.* Springer; New York: 1996.
25. Munroe, ME. *Theory of probability.* McGraw-Hill; New York: 1951.
26. Feller, W. *An introduction to probability theory and its applications.* Wiley; New York: 1967.
27. Frank LR. Anisotropy in high angular resolution diffusion-weighted mri. *Magn Reson Med.* 2001; 45(6):935–939. [PubMed: 11378869]
28. Assaf Y, Basser P. Composite hindered and restricted model of diffusion (charmed) mr imaging of the human brain. *Neuroimage.* 2005; 27(1):48–58. [PubMed: 15979342]
29. Tournier JD, Calamante F, Gadian DG, Connelly A. Direct estimation of the fiber orientation density function from diffusion-weighted mri data using spherical deconvolution. *Neuroimage.* 2004; 23(3):1176–1185. [PubMed: 15528117]
30. Ozarslan E, Shepherd TM, Vemuri BC, Blackband SJ, Mareci TH. Resolution of complex tissue microarchitecture using the diffusion orientation transform (dot). *Neuroimage.* 2006; 31(3):1086–1103. [PubMed: 16546404]
31. Özarslan E, Mareci TH. Generalized diffusion tensor imaging and analytical relationships between diffusion tensor imaging and high angular resolution diffusion imaging. *Magn Reson Med.* 2003; 50(5):955–965. [PubMed: 14587006]
32. Liu C, Bammer R, Acar B, Moseley ME. Characterizing non-gaussian diffusion by using generalized diffusion tensors. *Magn Reson Med.* 2004; 51(5):924–937. [PubMed: 15122674]
33. Jensen JH, Helpert JA, Ramani A, Lu H, Kaczynski K. Diffusional kurtosis imaging: The quantification of non-gaussian water diffusion by means of magnetic resonance imaging. *Magn Reson Med.* 2005; 53(6):1432–1440. [PubMed: 15906300]
34. Wedeen VJ, Hagmann P, Tseng WY, Reese TG, Weisskoff RM. Mapping complex tissue architecture with diffusion spectrum magnetic resonance imaging. *Magn Reson Med.* 2005; 54(6): 1377–1386. [PubMed: 16247738]
35. Tuch DS, Reese TG, Wiegell MR, Wedeen VJ. Diffusion mri of complex neural architecture. *Neuron.* 2003; 40(5):885–895. [PubMed: 14659088]
36. Papadakis NG, Xing D, Huang CL, Hall LD, Carpenter TA. A comparative study of acquisition schemes for diffusion tensor imaging using mri. *J Magn Reson.* 1999; 137(1):67–82. [PubMed: 10053134]
37. Özcan A. (mathematical) necessary conditions for the selection of gradient vectors in dti. *J Magn Reson.* 2005; 172(2):238–241. [PubMed: 15649751]

38. Özcan A. Minimization of imaging gradient effects in diffusion tensor imaging. *Medical Imaging, IEEE Transactions on*. 2011; 30(3):642–654.
39. Özcan A. Characterization of imaging gradients in diffusion tensor imaging. *J Magn Reson*. 2010; 207(1):24–33. [PubMed: 20810298]
40. Özcan A. Noise and nonlinear estimation with optimal schemes in dti. *Magn Reson Imaging*. 2010; 28(9):1335–1343. [PubMed: 20655681]
41. Basser PJ, Pierpaoli C. Microstructural and physiological features of tissues elucidated by quantitative-diffusion-tensor mri. *J Magn Reson B*. 1996; 111(3):209–219. [PubMed: 8661285]
42. Pajevic S, Pierpaoli C. Color schemes to represent the orientation of anisotropic tissues from diffusion tensor data: Application to white matter fiber tract mapping in the human brain. *Magn Reson Med*. 1999; 42(3):526–540. [PubMed: 10467297]
43. Jian B, Vemuri BC, Ozarslan E, Carney PR, Mareci TH. A novel tensor distribution model for the diffusion-weighted mr signal. *Neuroimage*. 2007; 37(1):164–176. [PubMed: 17570683]
44. Özcan A. A new model for diffusion weighted mri: Complete fourier direct mri. *Conf Proc IEEE Eng Med Biol Soc*. 2010; 2010:2710–2713. [PubMed: 21096205]
45. Özcan, A. Comparison of the complete fourier direct mri with existing diffusion weighted mri methods. *Biomedical Imaging: From Nano to Macro, 2011 IEEE International Symposium on*; 2011. p. 931-934.
46. Özcan, A.; Quirk, JD.; Wang, Y.; Wang, Q.; Sun, P.; Spees, WM.; Song, S-K. The validation of complete fourier direct mr method for diffusion mri via biological and numerical phantoms. *Proceedings of the 33st Annual International Conference of the IEEE EMB Society*; 2011. p. 3756-3759.

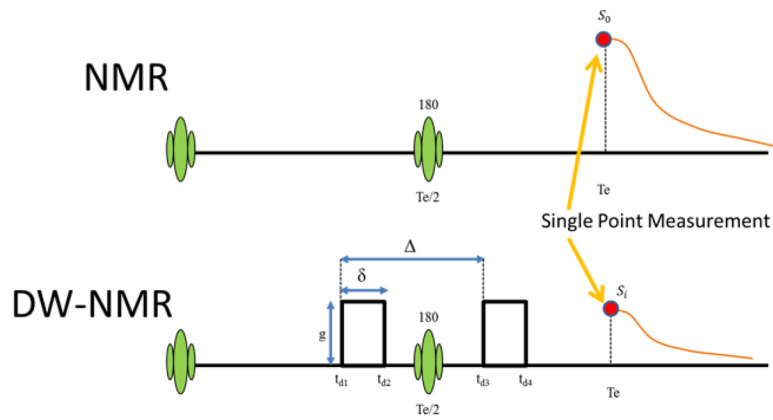


Figure 1. Spin echo (top) and Pulsed Gradient Spin Echo experiments. Diffusion sensitizing gradients are placed around the 180 degree radio frequency (RF) pulse. The duration and the separation of the pulses are δ and Δ respectively. The echo time is denoted by T_e and the measurement is the attenuation of the single point, the maximum of FID.

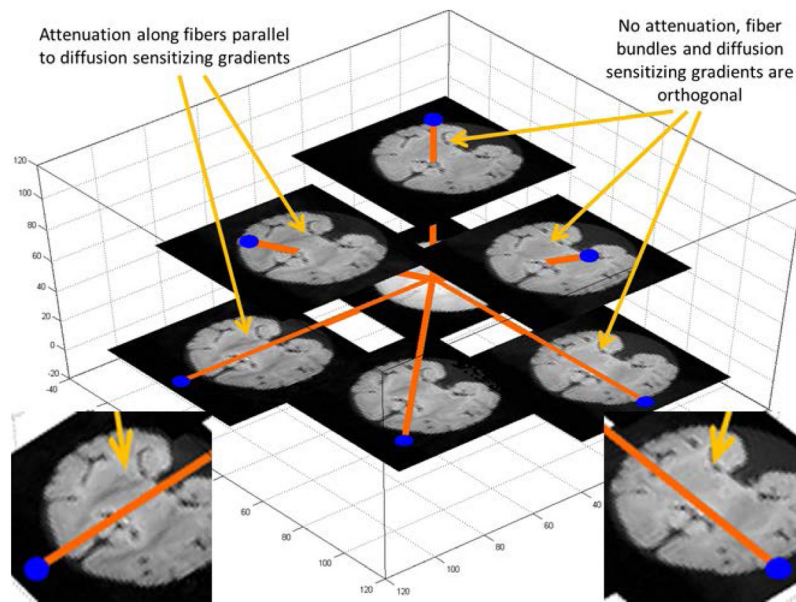


Figure 2. Diffusion weighted images from a PGSE experiment of an ex-vivo baboon brain [39, 40, 38] shown on top of the diffusion sensitizing gradient vectors (orange vectors with blue ends) of the diffusion gradient scheme (DGS). The image at the origin is acquired without diffusion gradients and therefore is unattenuated. The attenuation is highest on the fibers parallel to the diffusion gradient vector as shown in two zoomed images on the left and right bottom.

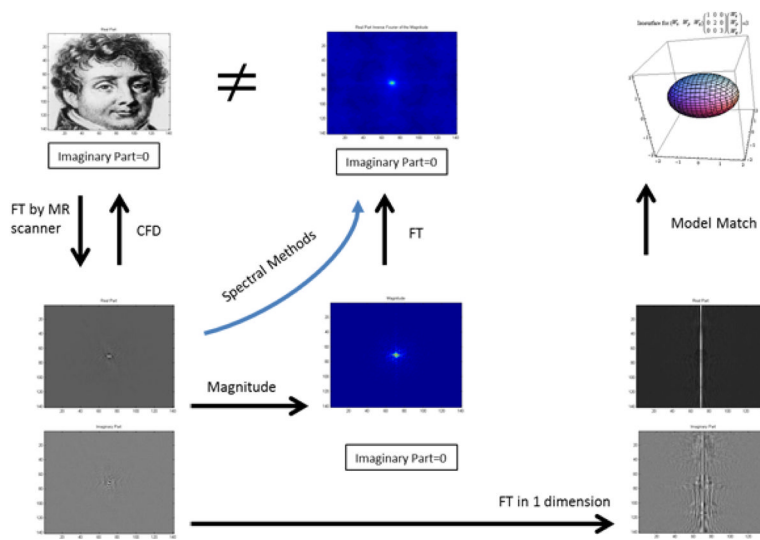


Figure 3. The summary of the DW methods is shown using the Fourier transform of Fourier’s portrait on top right corner. MR scanner takes the full Fourier transform of the portrait. CFD-MRI reconstructs the portrait by using the inverse transform. Spectral methods take the magnitude of the transform and compute the inverse transform. The outcome, shown in the middle column on top, does not resemble the original portrait. Model matching methods (arrow at the bottom) evaluate the inverse transform and work in a mixed physical-frequency space.